OFDM Radar With Subcarrier Aliasing—Reducing the ADC Sampling Frequency Without Losing Range Resolution

Oliver Lang, *Member, IEEE*, Reinhard Feger, Christian Hofbauer, *Member, IEEE*, and Mario Huemer, *Senior Member, IEEE*

***Abstract*—Many radar applications require a high range resolution, entailing the necessity for a large signal bandwidth. When employing an orthogonal frequency-division multiplexing (OFDM) radar system in its standard implementation, the radar system must operate at a high sampling frequency to ensure covering the entire signal bandwidth, thus imposing significant challenges on its implementation. Therefore, methods for reducing the sampling frequency are topic of recent research. In this work, a method for reducing the analog-to-digital converter (ADC) sampling frequency at the receiver without losing range resolution is proposed. This is achieved by activating only a fraction of the subcarriers at the transmitter, while simultaneously allowing for systematic aliasing due to undersampling in the receiver. This aliasing is designed such that the active subcarriers do not interfere with each other, which ensures a simple separation of them in the frequency domain. The proposed concept, denoted as subcarrier aliasing (SA), allows reducing the ADC sampling frequency in the receiver, but lacks in reducing the digital-to-analog converter (DAC) sampling frequency in the transmitter. However, the key asset of SA-OFDM lies in the properties of its waveform, making it especially suitable for joint radar and communication applications over other waveforms, e.g., stepped-carrier OFDM.**

***Index Terms*—ADC sampling frequency, ADC sampling rate, communications, OFDM radar, radar.**

I. Introduction

JOINT radar and communication systems are an active field of research with many potential applications, including automotive vehicle-to-vehicle communication. Orthogonal frequency-division multiplexing (OFDM) [1]–[10] is a promising waveform candidate for such systems, since it can be employed for the radar sensing and the communication task.

Manuscript received 2 October 2021; revised 19 February 2022 and 5 May 2022; accepted 5 June 2022. Date of publication 5 July 2022; date of current version 17 October 2022. This work was supported by Silicon Austria Labs (SAL), owned by the Republic of Austria, the Styrian Business Promotion Agency (SFG), the federal state of Carinthia, the Upper Austrian Research (UAR), and the Austrian Association for the Electric and Electronics Industry (FEEI). The review of this article was coordinated by Prof. Wan Choi. *(Corresponding author: Oliver Lang.)*

Oliver Lang and Mario Huemer are with the Institute of Signal Processing, Johannes Kepler University, 4040 Linz, Austria (e-mail: oliver.lang@jku.at; mario.huemer@jku.at).

Reinhard Feger is with the Institute for Communications Engineering and RF-Systems, Johannes Kepler University, 4040 Linz, Austria (e-mail: reinhard.feger@jku.at).

Christian Hofbauer is with the Silicon Austria Labs GmbH, 4040 Linz, Austria (e-mail: christian.hofbauer@silicon-austria.com).

Digital Object Identifier 10.1109/TVT.2022.3188511

An OFDM waveform features the following main system parameters [11]: the signal bandwidth B, the number of subcarriers N_c, the number of consecutively transmitted OFDM symbols N_sym, the carrier frequency f_c, and the length of the cyclic prefix (CP) T_cp. These system parameters determine the performance measures of the radar system [11], namely: the maximum unambiguous range r_max, the range resolution Δr, the maximum unambiguous relative velocity v_max, and the velocity resolution Δv. In its standard implementation [3], these performance measures are given by [11]

$$\Delta r = \frac{c_0}{2B} \qquad \Delta v = \frac{c_0}{2 f_\mathrm{c} N_\mathrm{sym} (T_0 + T_\mathrm{cp})} \tag{1}$$

$$r_\mathrm{max} = \Delta r N_\mathrm{c} \qquad v_\mathrm{max} = \pm \Delta v \frac{N_\mathrm{sym}}{2}, \tag{2}$$

where c_0 is the speed of light, $T_0 = 1/\Delta f = (N_\mathrm{c} - 1)/B$ is the duration of one OFDM symbol, and Δf represents the subcarrier spacing.

For many applications, the design of an analog-to-digital converter (ADC) for OFDM radar systems is a challenging task. One can identify at least three crucial requirements for the ADC design: 1) The ADC should have a high dynamic range to resolve strong nearby objects as well as weak distant objects. 2) The ADC should offer a high linearity to prevent an increase of the noise floor as well as ghost objects. 3) The ADC sampling frequency f_s must be high enough to cover the entire signal bandwidth B. The latter one is discussed in more detail in the following.

The signal bandwidth B solely determines the range resolution Δr, cf. (1). For instance, a desired range resolution of $\Delta r = 15\,\mathrm{cm}$ requires a bandwidth of $B = 1\,\mathrm{GHz}$. In a standard receiver, the ADC sampling frequency is low-bounded by $f_\mathrm{s} \geq B$, which entails the necessity of a very high-speed ADC for applications requiring a high range resolution.

The design and implementation of a very high-speed ADC is undoubtedly a challenging task and thus requires approaches to handle this. Several methods for reducing the ADC sampling frequency without sacrificing range resolution are proposed in the literature. One possible approach is to sample the entire bandwidth B sequentially rather than at once. This can be done by transmitting OFDM blocks with a lower bandwidth at different carrier frequencies either step-wise [12]–[21], denoted as stepped-carrier OFDM, or even continuously [22]. The

advantage of a reduced ADC sampling frequency offered by stepped-carrier OFDM comes along with some drawbacks. For instance, the maximum unambiguous velocity $v_{\max}$ is reduced due to the transmission of the sequential transmission of the blocks and due to an additional phase-locked loop (PLL) settling time between the blocks [13]. Another disadvantage arises for the communication task, where the repeatedly changing carrier frequency complicates synchronizing transmitter and communication receiver. Another approach to reduce the ADC sampling frequency is denoted as frequency comb OFDM radar [23], [24] and utilizes a comb of carrier frequencies simultaneously for up- and down-conversion of a baseband signal with a lower bandwidth. Unfortunately, generating a comb of carrier frequencies implies a significantly increased hardware complexity.

In this work, a novel OFDM joint radar and communication system is proposed which allows reducing the ADC sampling frequency without sacrificing range resolution. This not only eases the design and implementation of the ADC, but also the design and implementation of the receiver signal processing blocks, since they can be run at a reduced processing speed. These advantages are achieved at the cost of a reduced processing gain compared to a standard OFDM system due to the reduced number of available ADC samples. The method proposed in this work is denoted as subcarrier aliasing (SA), and the resulting waveform is denoted as SA-OFDM. The proposed joint radar and communication system based on the SA method is simply referred to as SA-OFDM radar system for discussions concerning the radar sensing task, and as SA-OFDM communication system for discussions regarding the communication task.

For SA, only a fraction of the subcarriers are active at the transmitter. All other subcarriers are zero subcarriers with no transmit energy. On the receiver side, the ADC uses a reduced sampling frequency $f_\mathrm{s} < B$ and thus introduces aliasing of the receive signal. However, aliasing is introduced in a systematic and controlled matter, such that the affected active subcarriers appear at the positions of originally zero subcarriers and thus do not interfere each other. Hence, the active subcarriers can be easily separated in frequency domain.

Please note that stepped-carrier OFDM allows reducing the sampling frequency of the digital-to-analog converter (DAC) in the transmitter and the ADC in the receiver. This is a clear advantage of stepped-carrier OFDM over SA-OFDM, which only allows reducing the ADC sampling frequency. However, a clear disadvantage of stepped-carrier OFDM is the resulting difficulties for the communication task in a joint radar sensing and communication application. As will be discussed in this work, repeatedly changing the carrier frequency complicates synchronization between the transmitter and the communication receiver. Possible approaches to allow for a constant carrier frequency at the communication receiver either require an ADC covering the whole signal bandwidth, or reduce the data rate (cf. Section V). In contrast to that, SA-OFDM is ideally suited for the communication task. In fact, it will turn out that the communication signal model for SA-OFDM can be formulated to match that for OFDM. This allows employing well-known methods for synchronization, channel estimation, and data estimation designed for OFDM communication systems also for SA-OFDM communication systems.

The analysis carried out in this work is briefly described in the following.

- The signal model and the receiver signal processing scheme for an SA-OFDM radar system is derived.
- The performance of the SA-OFDM radar system is investigated by evaluating the peak-to-average power ratio (PAPR), the processing gain, and the signal-to-noise ratio (SNR) in the range-Doppler map (RDM).
- Measurement results for an SA-OFDM radar system are presented and analyzed.
- Transmitter and receiver signal processing schemes for an SA-OFDM communication system are proposed.
- The SA-OFDM transmitter and receiver signal processing schemes are incorporated in a complete communication system including methods for channel estimation, synchronization, and data estimation.
- Finally, the bit error ratio (BER) performance of an SA-OFDM communication system is compared with that of a standard OFDM communication system via simulations.

This paper is organized as follows. Section II recaps the OFDM radar signal model, which is then used for the derivation of the proposed SA-OFDM radar system in Section III. This radar system is discussed and analyzed in Section IV. A comparison to stepped-carrier OFDM and frequency comb OFDM is carried out in Section V. Section VI presents the measurement results for an SA-OFDM radar system. The SA-OFDM communication system is proposed and discussed in Section VII. The BER simulations are presented in Section VIII, and finally, Section IX concludes this work.

Notation: Lower-case bold face variables ($\mathbf{a}$, $\mathbf{b}$,...) indicate vectors, and upper-case bold face variables ($\mathbf{A}$, $\mathbf{B}$,...) indicate matrices. We further use $\mathbb{N}$, $\mathbb{R}$, and $\mathbb{C}$ to denote the set of natural, real and complex numbers, respectively, $(\cdot)^T$ to denote transposition, $(\cdot)^*$ to denote the complex conjugation, and $(\cdot)^H$ to denote conjugate transposition. $\mathbf{I}^n$ refers to an identity matrix of size $n \times n$. $\mathbf{1}^n$ indicates a column vector of length n with all elements being one, $\oslash$ represents the element-wise division, and j represents the imaginary unit. The floor and ceil rounding operations are indicated via $\lfloor\cdot\rfloor$ and $\lceil\cdot\rceil$, respectively. The kth element of a vector is denoted as $[\cdot]_k$. The element of a matrix at the kth row and the lth column is indicated as $[\cdot]_{k,l}$, and $\%$ denotes the modulo operation.

Definitions: The discrete Fourier transform (DFT) matrix of size $N \times N$ is denoted as $\mathbf{F}_N \in \mathbb{C}^{N\times N}$, and its elements are given by $[\mathbf{F}_N]_{k,l} = \exp(-\mathrm{j}2\pi kl/N)$ with $l, k = 0, \ldots, N-1$. The frequently used vector $\mathbf{d}_N(f)$ containing a complex-valued oscillation is given as

$$\mathbf{d}_N(f) = \begin{bmatrix} 1 & \mathrm{e}^{\mathrm{j}2\pi f} & \ldots & \mathrm{e}^{\mathrm{j}2\pi f(N-1)} \end{bmatrix}^T \in \mathbb{C}^N, \quad (3)$$

where f is a unitless place-holder variable. A diagonal matrix with the elements of $\mathbf{d}_N(f)$ on its main diagonal is defined as $\mathbf{D}_N(f) = \mathrm{diag}(\mathbf{d}_N(f))$. The DFT of vector $\mathbf{d}_N(f)$ can be

expressed as $\mathbf{F}_N \mathbf{d}_N(f)$. Usually, windowed DFTs are preferred to reduce sidelobes. Let $\mathbf{w}_N \in \mathbb{R}^N$ be the window function of length N, then, the windowed DFT of vector $\mathbf{d}_N(f)$ is given by [4]

$$\mathbf{u}_N(f) = \mathbf{F}_N \operatorname{diag}(\mathbf{w}_N)\, \mathbf{d}_N(f) \tag{4}$$

$$= \begin{bmatrix} \sum_{n=0}^{N-1} [\mathbf{w}_N]_n \, \mathrm{e}^{\mathrm{j}2\pi(f-\frac{0}{N})n} \\ \vdots \\ \sum_{n=0}^{N-1} [\mathbf{w}_N]_n \, \mathrm{e}^{\mathrm{j}2\pi(f-\frac{N-1}{N})n} \end{bmatrix} \in \mathbb{C}^N. \tag{5}$$

II. OFDM Radar Signal Model

SA-OFDM is derived based on the OFDM signal model introduced in [4], which will be briefly repeated in this section. We refer to [4] for the complete derivation and all details. Overall, the reader is assumed to be familiar with the basic principles behind the OFDM waveform [4], [25].

The OFDM waveform consists of N_c subcarriers in the frequency domain. These N_c subcarriers are equidistantly allocated within a bandwidth B, resulting in a subcarrier spacing of $\Delta f = B/N_\mathrm{c}$. The complex-valued amplitude values of the subcarriers are referred to as subcarrier symbols. These subcarrier symbols are usually drawn from a symbol alphabet, e.g., the quadrature phase-shift keying (QPSK) symbol alphabet. Let $\mathbf{S} \in \mathbb{C}^{N_\mathrm{c} \times N_\mathrm{sym}}$ contain the subcarrier symbols for all N_c subcarriers and for all N_sym consecutively transmitted OFDM symbols. Each row of $\mathbf{S}$ represents a subcarrier, and each column of $\mathbf{S}$ represents an OFDM symbol. The corresponding time domain OFDM symbols are obtained by applying an inverse discrete Fourier transform (IDFT) of length N_c on the columns of $\mathbf{S}$. The duration of these time domain OFDM symbols is $T = 1/\Delta f = N_\mathrm{c}/f_\mathrm{s}$. Adding the CP of length T_cp extends the signal duration to $T_\mathrm{OFDM} = T + T_\mathrm{cp}$.

The radio frequency (RF) transmit signal is obtained by modulating the OFDM time domain signal onto a carrier frequency f_c. The corresponding receive signal consists in general of multiple delayed and damped copies of the transmit signal originating from different propagation paths between a transmit and receive antenna. The number of propagation paths is denoted as N_path. The propagation distance for the ith path is denoted as r_i with $0 \leq i < N_\mathrm{path}$. The corresponding round-trip delay time is given by $\tau_i = 2r_i/c_0$. The so-called normalized time delay is defined as $\bar{\tau}_i = \tau_i \Delta f$. A potential relative velocity along the ith path is denoted as v_i. This relative velocity causes a Doppler shift of $f_{\mathrm{D}_i} = -2v_i f_\mathrm{c}/c_0$, which is normalized to $\bar{f}_{\mathrm{D}_i} = f_{\mathrm{D}_i}/\Delta f$.

The matrix $\mathbf{Y}_\mathrm{tf,ts} \in \mathbb{C}^{N_\mathrm{c} \times N_\mathrm{sym}}$ contains the received time domain OFDM symbols after demodulation with the carrier frequency f_c and removal of the CP. This matrix is given by [4]

$$\mathbf{Y}_\mathrm{tf,ts} = \sum_{i=0}^{N_\mathrm{path}-1} \bar{a}_i \mathbf{D}_{N_\mathrm{c}}\left(\frac{\bar{f}_{\mathrm{D}_i}}{N_\mathrm{c}}\right) \mathbf{F}_{N_\mathrm{c}}^{-1} \mathbf{D}_{N_\mathrm{c}}^*(\bar{\tau}_i) \mathbf{S} \mathbf{D}_{N_\mathrm{sym}}(\bar{f}_{\mathrm{D}_i}\alpha), \tag{6}$$

where tf and ts stand for fast time and slow time, respectively, and where the noise term is neglected. The expression in (6) is discussed in the following. The frequency domain OFDM symbols in $\mathbf{S}$ are transformed into time domain via multiplication with $\mathbf{F}_{N_\mathrm{c}}^{-1}$ from the left. The delay due to propagation is modelled in frequency domain via $\mathbf{D}_{N_\mathrm{c}}^*(\bar{\tau}_i)$. The quantity $\alpha \in \mathbb{R}$ is defined as $\alpha = (T + T_\mathrm{cp})/T$. $\bar{a}_i$ in (6) is defined as $\bar{a}_i = a_i \cdot \exp(-\mathrm{j}2\pi f_\mathrm{c} \tau_i)$, where $a_i \in \mathbb{C}$ models an assumed constant amplitude and phase change for the ith path. The distortions caused by the Doppler shift are modelled in form of a common phase error (CPE) and inter-carrier interference (ICI) [4]. The CPE is represented by $\mathbf{D}_{N_\mathrm{sym}}(\bar{f}_{\mathrm{D}_i}\alpha)$, and the ICI effect modelled by $\mathbf{D}_{N_\mathrm{c}}\left(\frac{\bar{f}_{\mathrm{D}_i}}{N_\mathrm{c}}\right)$. To simplify matters, the ICI term is neglected for the mathematical derivations for convenience, but it will be included for all simulations.

On basis of the model in (6), the proposed SA-OFDM joint radar and communication system is derived in the sequel. Section III–VI investigate SA-OFDM in the context of radar sensing, while Section VII and Section VIII focus on aspects in the context of communications.

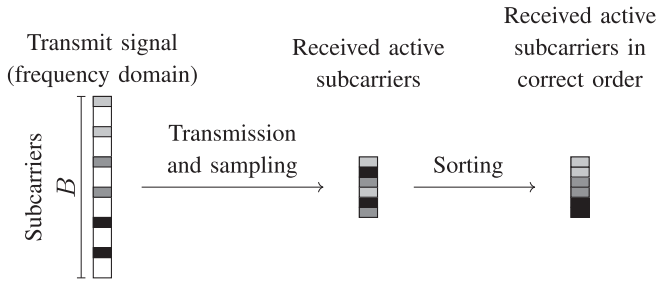

Fig. 1. Schematic visualization of the working principle of SA-OFDM.

III. Subcarrier-Aliasing OFDM Radar System

Fig. 1 sketches the basic principle of SA-OFDM. There, the left bar represents a transmit OFDM symbol in frequency domain. Within this OFDM symbol, only every μth subcarrier with $\mu \in \mathbb{N}^+$ is chosen to be an active subcarrier (gray blocks). Between these active subcarriers, there are $\mu - 1$ zero subcarriers with no transmit energy (white boxes). On the receiver side, the ADC uses a reduced sampling frequency $f_\mathrm{s} < B$ and thus introduces aliasing of the receive signal. This aliasing causes the affected active subcarriers to appear at the positions of originally zero subcarriers, such that they do not interfere each other. Hence, the active subcarriers can be easily separated in frequency domain (middle bar in Fig. 1). Aliasing changes the order of the active subcarriers observed at the receiver in comparison to the transmit signal. However, this can easily be compensated by a re-ordering step in the receiver (right bar in Fig. 1).

Fig. 2 shows the basic radar signal processing scheme for an SA-OFDM radar system, which will be discussed in the following.

Transmit signal: Recall that $\mathbf{S}$ contains the subcarrier symbols for all N_c subcarriers and for all N_sym OFDM symbols. In SA-OFDM, only every μth subcarrier is a so-called active subcarrier with $\mu \in \mathbb{N}^+$. The number of active subcarriers is denoted as N_a and can be derived according to $N_\mathrm{a} = \left\lceil \frac{N_\mathrm{c}}{\mu} \right\rceil$. All other subcarriers are zero subcarriers with no transmit energy. Loading

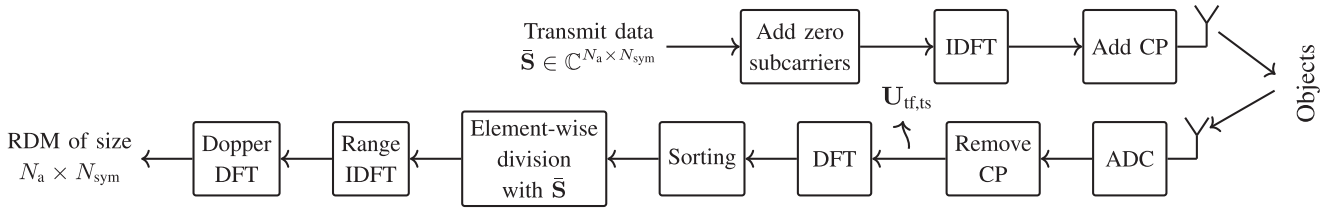

Fig. 2. Visualization of the radar signal processing for an SA-OFDM radar system. The analog front-end and the parallel-to-serial conversion are not shown for the sake of brevity.

of the active subcarriers and inserting the zero subcarriers in $\mathbf{S}$ is mathematically described by

$$\mathbf{S} = \mu \mathbf{B}_z \bar{\mathbf{S}}, \tag{7}$$

where $\bar{\mathbf{S}} \in \mathbb{C}^{N_a \times N_{sym}}$ contains the subcarrier symbols for the active subcarriers, and where $\mathbf{B}_z \in \mathbb{C}^{N_c \times N_a}$ inserts $\mu - 1$ zero subcarriers between the active subcarriers. In this work, it is assumed that $\mathbf{B}_z$ is designed such that the first subcarrier represented by the top row of $\mathbf{S}$ is an active subcarrier. Formally, only activating every μth subcarrier reduces the average power of the time domain transmit signal by a factor of μ according to Parseval's theorem. Thus, μ is introduced in (7) to prevent this reduction of the average transmit power.

Receive signal: The receiver uses a reduced ADC sampling frequency such that $f_s < B$. For the sake of simplicity, let us assume $f_s = \frac{B}{\kappa}$ with $\kappa \in \mathbb{N}^+$. Then, the sampling process can be modelled by taking only every κth sample from (6). This can be described by employing a selection matrix $\mathbf{B}_s \in \mathbb{C}^{N_s \times N_c}$, which selects every κth sample beginning with the first one. The number of ADC samples obtained this way is given by $N_s = \left\lceil \frac{N_c}{\kappa} \right\rceil$. Now, the receive signal for SA-OFDM follows from inserting (7) into (6),[1] and employing the selection matrix $\mathbf{B}_s$, yielding

$$\mathbf{U}_{tf,ts} = \sum_{i=0}^{N_{path}-1} \mu \bar{a}_i \mathbf{B}_s \mathbf{F}_{N_c}^{-1} \mathbf{D}_{N_c}^{*}(\bar{\tau}_i) \mathbf{B}_z \bar{\mathbf{S}} \mathbf{D}_{N_{sym}}(\bar{f}_{D_i} \alpha), \tag{8}$$

DFT along columns: The receive signal in frequency domain is obtained by applying a DFT of length N_s on the columns of $\mathbf{U}_{tf,ts}$ in (8), yielding

$$\mathbf{U}_{f,ts} = \mathbf{F}_{N_s} \mathbf{U}_{tf,ts} \tag{9}$$

$$= \sum_{i=0}^{N_{path}-1} \mu \bar{a}_i \mathbf{F}_{N_s} \mathbf{B}_s \mathbf{F}_{N_c}^{-1} \mathbf{D}_{N_c}^{*}(\bar{\tau}_i) \mathbf{B}_z \bar{\mathbf{S}} \mathbf{D}_{N_{sym}}(\bar{f}_{D_i} \alpha). \tag{10}$$

The goal of this processing step is to recover the received active subcarriers. This requires that each of the N_s frequency bins is occupied by at most one active subcarrier, which is ensured, if two constraints are fulfilled.

The first constraint is that N_c must be an integer multiple of κ. Otherwise, the active subcarriers would be placed "in between" the frequency bins, causing severe windowing effects due to loss of orthogonality. This effect is clarified in Fig. 3, which shows the time domain signal for the real part of an arbitrary

[1] and neglecting the ICI term as already discussed.

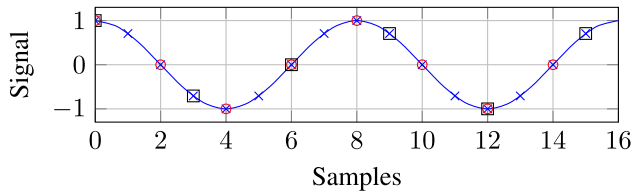

Fig. 3. Time domain signal of the real part of a subcarrier over two periods and 16 samples (blue crosses). The samples obtained with a reduced sampling frequency are indicated for $\kappa = 2$ (red circles) and for $\kappa = 3$ (black squares).

received subcarrier. The $N_s = N_c = 16$ ADC samples obtained for $\kappa = 1$ are marked with blue crosses. Comparing the signal at the left and the right border shows that it can be interpreted as a circular periodic signal, and thus, the corresponding frequency domain representation is a single Dirac peak located on a DFT bin without any windowing effects. Now, reducing the ADC sampling frequency, e.g., by a factor $\kappa = 2$ (red crosses) delivers again a circular periodic signal such that its frequency transform is a single Dirac peak at a DFT bin. However, reducing the ADC sampling frequency by a factor of $\kappa = 3$, and thus $N_c/\kappa \neq \mathbb{N}^+$, yields the signal indicated with black squares. This signal is not circular periodic anymore, and so, severe windowing effects are observed in frequency domain. This is why we choose N_c to be an integer multiple of κ. With this choice, the number of ADC samples N_s modifies to $N_s = \left\lceil \frac{N_c}{\kappa} \right\rceil = \frac{N_c}{\kappa}$.

The second constraint ensures suitable combinations of μ, κ, and N_c for SA-OFDM. Non-appropriate combinations may result in two or more active subcarriers occupying the same frequency bin in (10) due to aliasing. Whether this is the case or not can be clarified in the following way. Removing all terms modelling the propagation paths from (10), and replacing $\bar{\mathbf{S}}$ by $\mathbf{1}^{N_a}$ such that a one is transmitted on all N_a active subcarriers, yields

$$\mathbf{t}_1 = \frac{N_c}{N_s} \mathbf{F}_{N_s} \mathbf{B}_s \mathbf{F}_{N_c}^{-1} \mathbf{B}_z \mathbf{1}^{N_a} \in \mathbb{C}^{N_s}, \tag{11}$$

where the factor N_c/N_s accounts for a scaling introduced by $\mathbf{F}_{N_s}$ and $\mathbf{F}_{N_c}^{-1}$. If $\mathbf{t}_1$ consists of N_a ones and $N_s - N_a$ zeros, then every frequency bin is occupied by at most one active subcarrier. Zeros in $\mathbf{t}_1$ indicate frequency bins not occupied by any active subcarrier. A value larger than 1 as well as a complex value in $\mathbf{t}_1$ would indicate that two or more active subcarriers are occupying the same frequency bin. Alg. 1 shows a systematic approach for finding a suitable μ for given values of κ and N_c based on evaluating (11). μ_{max} serves as a stopping criterion in case no suitable combination of μ, κ, and N_c can be found.

Algorithm 1: Find suitable μ for SA-OFDM.

Input: κ, N_c, μ_max;
Initialization:
  $N_\mathrm{s} = \frac{N_\mathrm{c}}{\kappa}$;
  Construct $\mathbf{F}_{N_\mathrm{s}}$, $\mathbf{B}_\mathrm{s}$ and $\mathbf{F}_{N_\mathrm{c}}^{-1}$;
for $\mu = \kappa, \kappa+1, \ldots, \mu_\mathrm{max}$ **do**
  $N_\mathrm{a} = \left\lceil \frac{N_\mathrm{c}}{\mu} \right\rceil$;
  Construct $\mathbf{B}_\mathrm{z}$;
  Derive $\mathbf{t}_1 = \frac{N_\mathrm{c}}{N_\mathrm{s}} \mathbf{F}_{N_\mathrm{s}} \mathbf{B}_\mathrm{s} \mathbf{F}_{N_\mathrm{c}}^{-1} \mathbf{B}_\mathrm{z} \mathbf{1}^{N_\mathrm{a}}$;
  if $\mathbf{t}_1$ contains N_a ones and $N_\mathrm{s} - N_\mathrm{a}$ zeros **then**
    return μ.
  end
end

Sorting: Naturally, with aliasing comes a distorted order of the active subcarriers compared to the transmit signal. In this processing step, the active subcarriers are re-sorted to obtain the correct order.

A pragmatic approach for identifying the observed order of active subcarriers is based on (11), except that $\mathbf{1}^{N_\mathrm{a}}$ is replaced by $\begin{bmatrix} 1 & 2 & \ldots & N_\mathrm{a} \end{bmatrix}^T \in \mathbb{C}^{N_\mathrm{a}}$, with the result that a one is transmitted at the first active subcarrier, a two is transmitted on the second active subcarrier, and so on. Doing so yields

$$\mathbf{t}_2 = \frac{N_\mathrm{c}}{N_\mathrm{s}} \mathbf{F}_{N_\mathrm{s}} \mathbf{B}_\mathrm{s} \mathbf{F}_{N_\mathrm{c}}^{-1} \mathbf{B}_\mathrm{z} \begin{bmatrix} 1 & 2 & \ldots & N_\mathrm{a} \end{bmatrix}^T \in \mathbb{C}^{N_\mathrm{s}}. \quad (12)$$

The observed order of active subcarriers can then be seen in $\mathbf{t}_2$ and can further be used to construct a sorting matrix $\mathbf{B}_\mathrm{so} \in \mathbb{C}^{N_\mathrm{a} \times N_\mathrm{s}}$ that reconstructs the correct order of the received active subcarriers. Applying this sorting matrix on (10) yields

$$\mathbf{V}_\mathrm{f,ts} = \mathbf{B}_\mathrm{so} \mathbf{U}_\mathrm{f,ts} \quad (13)$$

$$= \sum_{i=0}^{N_\mathrm{path}-1} \mu \bar{a}_i \mathbf{B}_\mathrm{so} \mathbf{F}_{N_\mathrm{s}} \mathbf{B}_\mathrm{s} \mathbf{F}_{N_\mathrm{c}}^{-1} \mathbf{D}_{N_\mathrm{c}}^*(\bar{\tau}_i) \mathbf{B}_\mathrm{z} \bar{\mathbf{S}} \mathbf{D}_{N_\mathrm{sym}}(\bar{f}_{\mathrm{D}_i} \alpha), \quad (14)$$

which allows for some simplifications. First, the product $\mathbf{D}_{N_\mathrm{c}}^*(\bar{\tau}_i)\mathbf{B}_\mathrm{z}$ is inspected. $\mathbf{B}_\mathrm{z}$ adds $\mu - 1$ zero subcarriers between the active subcarriers, and $\mathbf{D}_{N_\mathrm{c}}^*(\bar{\tau}_i)$ applies a phase rotation on all subcarriers. The order of $\mathbf{D}_{N_\mathrm{c}}^*(\bar{\tau}_i)$ and $\mathbf{B}_\mathrm{z}$ can be exchanged when accounting for the zero subcarriers in $\mathbf{D}_{N_\mathrm{c}}^*(\bar{\tau}_i)$. Thus, it holds that $\mathbf{D}_{N_\mathrm{c}}^*(\bar{\tau}_i)\mathbf{B}_\mathrm{z} = \mathbf{B}_\mathrm{z}\mathbf{D}_{N_\mathrm{a}}^*(\mu\bar{\tau}_i)$, yielding

$$\mathbf{V}_\mathrm{f,ts} = \sum_{i=0}^{N_\mathrm{path}-1} \mu \bar{a}_i \mathbf{B}_\mathrm{so} \mathbf{F}_{N_\mathrm{s}} \mathbf{B}_\mathrm{s} \mathbf{F}_{N_\mathrm{c}}^{-1} \mathbf{B}_\mathrm{z} \mathbf{D}_{N_\mathrm{a}}^*(\mu\bar{\tau}_i) \bar{\mathbf{S}} \mathbf{D}_{N_\mathrm{sym}}(\bar{f}_{\mathrm{D}_i} \alpha). \quad (15)$$

Second, the term $\mathbf{B}_\mathrm{so}\mathbf{F}_{N_\mathrm{s}}\mathbf{B}_\mathrm{s}\mathbf{F}_{N_\mathrm{c}}^{-1}\mathbf{B}_\mathrm{z}$ turns out to be an identity matrix scaled by a factor $N_\mathrm{s}/N_\mathrm{c}$. Thus, (15) can be simplified to

$$\mathbf{V}_\mathrm{f,ts} = \sum_{i=0}^{N_\mathrm{path}-1} \mu \bar{a}_i \frac{N_\mathrm{s}}{N_\mathrm{c}} \mathbf{D}_{N_\mathrm{a}}^*(\mu\bar{\tau}_i) \bar{\mathbf{S}} \mathbf{D}_{N_\mathrm{sym}}(\bar{f}_{\mathrm{D}_i} \alpha). \quad (16)$$

Element-wise division: Dividing $\mathbf{V}_\mathrm{f,ts}$ in (16) element-wise by $\bar{\mathbf{S}}$ leads to

$$\mathbf{Z}_\mathrm{f,ts} = \mathbf{V}_\mathrm{f,ts} \oslash \bar{\mathbf{S}} \quad (17)$$

$$= \sum_{i=0}^{N_\mathrm{path}-1} \mu \bar{a}_i \frac{N_\mathrm{s}}{N_\mathrm{c}} \mathbf{D}_{N_\mathrm{a}}^*(\mu\bar{\tau}_i) \mathbf{1}^{N_\mathrm{a}} (\mathbf{1}^{N_\mathrm{sym}})^T \mathbf{D}_{N_\mathrm{sym}}(\bar{f}_{\mathrm{D}_i} \alpha), \quad (18)$$

where the identity $(\mathbf{D}_a \mathbf{M} \mathbf{D}_b) \oslash \mathbf{M} = \mathbf{D}_a \mathbf{1}^n (\mathbf{1}^m)^T \mathbf{D}_b$ was utilized, which holds for arbitrary matrices $\mathbf{M} \in \mathbb{C}^{n \times m}$ with non-zero elements, arbitrary diagonal matrices $\mathbf{D}_a \in \mathbb{C}^{n \times n}$ and $\mathbf{D}_b \in \mathbb{C}^{m \times m}$. Furthermore, employing the identity $\mathbf{d}_N(f) = \mathbf{D}_N(f)\mathbf{1}^N$ yields

$$\mathbf{Z}_\mathrm{f,ts} = \sum_{i=0}^{N_\mathrm{path}-1} \mu \bar{a}_i \frac{N_\mathrm{s}}{N_\mathrm{c}} \mathbf{d}_{N_\mathrm{a}}^*(\mu\bar{\tau}_i) \mathbf{d}_{N_\mathrm{sym}}(\bar{f}_{\mathrm{D}_i} \alpha)^T, \quad (19)$$

Range IDFT: Applying a windowed range IDFT defined in (4) results in

$$\mathbf{Z}_\mathrm{r,ts} = \mathbf{F}_{N_\mathrm{a}}^{-1} \mathbf{W}_{N_\mathrm{a}} \mathbf{Z}_\mathrm{f,ts} \quad (20)$$

$$= \sum_{i=0}^{N_\mathrm{path}-1} \mu \bar{a}_i \frac{N_\mathrm{s}}{N_\mathrm{c}} \mathbf{u}_{N_\mathrm{a}}^*(\mu\bar{\tau}_i) \mathbf{d}_{N_\mathrm{sym}}(\bar{f}_{\mathrm{D}_i} \alpha)^T. \quad (21)$$

Doppler DFT: Finally, applying a windowed Doppler DFT yields the desired RDM

$$\mathbf{Z}_\mathrm{r,v} = \mathbf{Z}_\mathrm{r,ts} \mathbf{W}_{N_\mathrm{sym}} \mathbf{F}_{N_\mathrm{sym}} \quad (22)$$

$$= \sum_{i=0}^{N_\mathrm{path}-1} \mu \bar{a}_i \frac{N_\mathrm{s}}{N_\mathrm{c}} \mathbf{u}_{N_\mathrm{a}}^*(\mu\bar{\tau}_i) \mathbf{u}_{N_\mathrm{sym}}(\bar{f}_{\mathrm{D}_i} \alpha)^T \quad (23)$$

of size $N_\mathrm{a} \times N_\mathrm{sym}$.

IV. Properties of SA-OFDM Radar Systems

The effects of SA-OFDM for the radar sensing task are compared with that of a standard OFDM radar system in the following.

A. Effects on the Range Resolution

According to (1), the range resolution Δr is determined by the bandwidth B. In many cases, SA-OFDM leaves the bandwidth unaltered compared to a standard OFDM radar system. Minor deviations only occur in case zero subcarriers lie at the borders of the bandwidth such as indicated in Fig. 1. The covered bandwidth is then

$$B_\mathrm{sa} = B \frac{\mu N_\mathrm{a}}{N_\mathrm{c}}, \quad (24)$$

and the range resolution changes to

$$\Delta r = \frac{c_0}{2 B_\mathrm{sa}}. \quad (25)$$

B. Effects on the Maximum Range

In a standard OFDM radar system, the maximum unambiguous range r_max scales with the number of subcarriers, cf. (2).

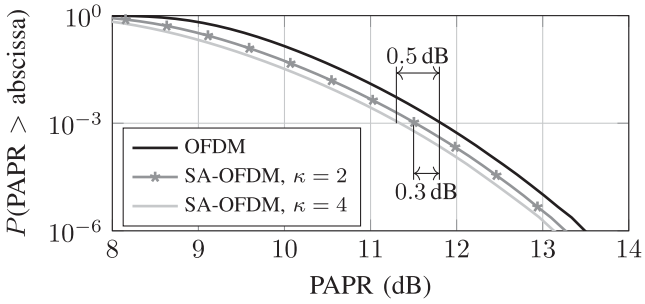

Fig. 4. CCDF of the PAPR for a standard OFDM transmit signal and for an SA-OFDM transmit signal with $\kappa = 2$ and $\kappa = 4$.

An SA-OFDM radar system utilizes only $N_\text{a} = \left\lceil \frac{N_\text{c}}{\mu} \right\rceil$ subcarriers out of N_c possible subcarriers. Therefore, the maximum unambiguous range reduces to

$$r_\text{max} = \Delta r N_\text{a}, \tag{26}$$

which is lower than the maximum unambiguous range obtained for a standard OFDM radar system by approximately a factor of μ. Whether this reduction is acceptable or not depends on the application as well as on the parametrization of the OFDM waveform [10], [11]. Note that objects with a high enough signal energy violating the maximum unambiguous range will reappear in the RDM as a ghost object.

C. Effects on the Maximum Velocity and Velocity Resolution

An SA-OFDM radar system offers the same maximum velocity v_max and velocity resolution Δv as a standard OFDM radar system.

D. Effects on the PAPR

The OFDM waveform is known to suffer from a high PAPR. In the following, the PAPR of the transmit signal generated by an SA-OFDM radar system is compared with that of a standard OFDM radar system. This comparison is carried out in form of the complementary cumulative distribution function (CCDF), which represents the probability for the PAPR being larger than the corresponding value at the horizontal axis [26]. This CCDF is evaluated for the baseband transmit signals with the method described in [26], with an oversampling factor of 4, and for QPSK subcarrier symbols. The utilized system parameters correspond to that detailed in Section VII. The resulting CCDFs are shown in Fig. 4, indicating that SA-OFDM reduces the PAPR. Specifically, for a CCDF value of 10^{-3}, the PAPR is reduced by 0.3 dB for $\kappa = 2$, and by 0.5 dB for $\kappa = 4$. The cause of this reduction is the reduced number of active subcarriers utilized by SA-OFDM.

E. Effects on the SNR At the ADC Input

Due to the additional factor of μ introduced in (7), the average transmit power of an SA-OFDM radar system and a standard OFDM radar system can be considered equal. It will be assumed that also the average receive power values for both radar systems are equal. With the additional assumption that both radar systems have equal noise bandwidths and noise power values, one can conclude that the SNR at the ADC input of the two radar systems is equal, too.

F. Effects on the SNR of the ADC Samples

The two radar systems feature different ADC sampling frequencies. However, when neglecting quantization noise, the SNR of the ADC samples is the same as the SNR at the input of the ADC independent of the sampling frequency. Hence, the SNR of the ADC samples is the same for an SA-OFDM radar system as for a standard OFDM radar system.

G. Effects on the Receiver Processing Gain

The range IDFT and the Doppler DFT have a length of N_a and N_sym. Hence, the receiver processing gain is given by $G_\text{p} = 10 \cdot \log_{10}(N_\text{sym} N_\text{a})$ dB. A standard OFDM radar system features a processing gain of $G_\text{p} = 10 \cdot \log_{10}(N_\text{sym} N_\text{c})$ dB, indicating that SA-OFDM decreases the processing gain by $10 \cdot \log_{10}(N_\text{a}/N_\text{c})$ dB.

H. Effects on the SNR in the RDM

The SNR in the final RDM is determined by the SNR in the ADC samples and the receiver processing gain. This directly leads to the conclusion that SA-OFDM decreases the SNR in the RDM by $10 \cdot \log_{10}(N_\text{a}/N_\text{c})$ dB.

I. Effects on Follow-Up Processing Steps

SA-OFDM does not only ease the design and implementation of the ADC, but also the design and implementation of many follow-up processing steps, since they can be run at the reduced frequency, too.

J. Effects of ICI on the SNR

It is well-known that a relative velocity of an object destroys the orthogonality of the subcarriers at the receiver, which leads to ICI. This ICI degrades the SNR in the RDM [4]. This degradation is analyzed via simulations in the following. For that, we assume a carrier frequency $f_\text{c} = 76.6\,\text{GHz}$, a bandwidth $B = 1\,\text{GHz}$, $N_\text{c} = 1024$ subcarriers, and $N_\text{sym} = 256$ OFDM symbols. The length of the CP is $T_\text{cp} = 1\,\mu\text{s}$ for all considered waveforms, although it could have been reduced for SA-OFDM due to its reduced maximum unambiguous range r_max. The radar scenario contains a single object ($N_\text{path} = 1$) at a distance of 10 m and with $a_0 = 10$. Additive measurement noise is dismissed such that ICI is the only source of noise. This ICI is caused by a relative velocity of the object, which is proportional to the normalized Doppler shift $\bar{f}_{\text{D}_i} = f_{\text{D}_i}/\Delta f$. The effect of ICI on the SNR is analyzed for

- a standard OFDM radar system,
- a stepped-carrier OFDM radar system with $N_\text{sb} = 2$ subbands,
- a stepped-carrier OFDM radar system with $N_\text{sb} = 4$ subbands,
- an SA-OFDM radar system with $\kappa = 2$ ($N_\text{a} = 342$), and
- an SA-OFDM radar system with $\kappa = 4$ ($N_\text{a} = 205$).

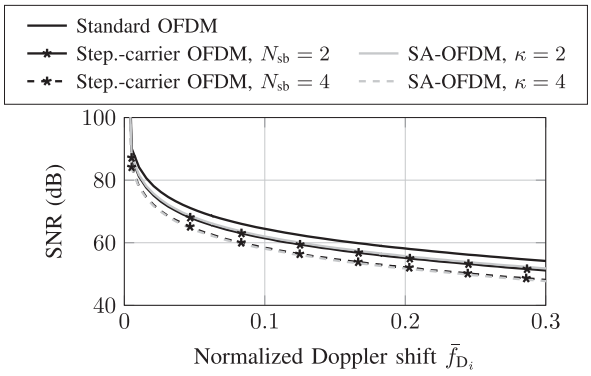

Fig. 5. SNR in the RDM plotted over the normalized Doppler shift $\bar{f}_{\mathrm{D}_i}$.

The values for N_{sb} are chosen such that the ADC sampling frequencies coincide with those of the SA-OFDM radar systems.

The SNR values are obtained by subtracting the noise floor from the dB value of the highest peak in the RDM. The noise floor is estimated as the median magnitude value of the RDM in dB. The SNR values obtained this way are shown in Fig. 5 in dependency of the normalized Doppler shift $\bar{f}_{\mathrm{D}_i}$. These curves show that the degradation of the SNR due to ICI is quite similar for all considered radar systems. The stepped-carrier OFDM radar systems have a loss in SNR of approximately 3 dB ($N_{\mathrm{sb}} = 2$), and approximately 6 dB ($N_{\mathrm{sb}} = 4$) compared to the standard OFDM radar system due to the reduced processing gains. Although the SA-OFDM radar systems have lower processing gains than the stepped-carrier OFDM radar systems, the SNR curves almost lie on top of each other. This is due to the fact that SA-OFDM (with this parametrization) contains zero subcarriers in the receive signal even after aliasing, which reduces the impact of ICI.

V. Comparison to Competitive OFDM-Based Radar Systems

In the sequel, the proposed SA-OFDM is compared to competitive radar systems allowing for a reduction of the ADC sampling frequency, too.

A. Stepped-Carrier OFDM Radar Systems

Stepped-carrier OFDM [12]–[19] measures a high bandwidth sequentially in blocks with a lower bandwidth, and allows for a reduced DAC sampling frequency in the transmitter, and for a reduced ADC sampling frequency in the receiver. In contrast to that, SA-OFDM only allows reducing the ADC sampling frequency in the receiver, while the DAC sampling frequency in the transmitter remains unaltered.

In general, the standard OFDM waveform is suited for joint radar sensing and communication applications, consequently also stepped-carrier OFDM can be deployed. However, the need for changing the carrier frequency in this approach raises some technical challenges, as the communication receiver is urged to follow this carrier frequency with its own PLL, which severely complicates synchronization and thus the design of the communication receiver.

A circumvention for this problem could be a limitation of the communication link to a single subband in the frequency domain. Then, the communication receiver could use a single constant carrier frequency for demodulation, but on the other hand would lead to long pauses within the receive signal, entailing a significant reduction of the achievable data rate. Due to the reduction to a single subband and the long pauses within the receive signal, the data rate would be reduced by a factor of $1/N_{\mathrm{sb}}^2$ compared to a standard OFDM system utilizing the full bandwidth, where N_{sb} denotes the number of subbands used by a stepped-carrier OFDM system. Compared to an SA-OFDM system providing the same reduction of the ADC sampling frequency, the data rate of the stepped-carrier OFDM system would be reduced approximately by a factor of $1/N_{\mathrm{sb}}$. The loss in data rate becomes even more when considering the settling-time of the PLL. In contrast to that, SA-OFDM is ideally suited for enabling communications in joint radar sensing and communication applications as will be shown in Section VII.

The next comparison focuses on the SNR in the RDM for the radar sensing task, whose outcome is not unambiguous and depends on the underlying terms. On the one hand, in case $\mu > \kappa$, the receive signal for SA-OFDM contains zero subcarriers even after aliasing, which decreases the SNR of an SA-OFDM radar system in relation to a stepped-carrier OFDM radar system. On the other hand, stepped-carrier OFDM additionally suffers from a PLL induced SNR loss, with the actual loss depending on the specific PLL and thus being hard to quantify. One reason is that stepped-carrier OFDM introduces unused time slots due to the settling-time of the PLL, which translates to an SNR loss compared to SA-OFDM when keeping the total measurement time constant for both methods, which seems to be a reasonable assumption for a fair comparison. A second reason is that in general designing a PLL with fast settling time negatively affects the achievable phase noise characteristics, which translates to an additional SNR reduction in the RDM [13]. Due to these reasons, a general statement about the SNR of SA-OFDM in comparison to the SNR of stepped-carrier OFDM is rather difficult to make and requires more assumptions on the hardware.

Stepped-carrier OFDM reduces the ADC sampling frequency at the cost of a reduced $v_{\max}$, while SA-OFDM reduces the ADC sampling frequency at the cost of a reduced $r_{\max}$. Which one of these circumstances infers more severe limitations depends on the application and on the parametrization of the OFDM waveform [10], [11].

Both systems also differ in terms of mutual interferences. Mutual interferences of different radar devices are considered as a major issue [27], [28]. For SA-OFDM systems, interferences within the complete bandwidth including all active subcarriers and all zero subcarriers have an influence on the radar system's performance. For stepped-carrier OFDM systems, only the part of the interference that falls within the currently covered subband influences the radar system's performance.

B. Frequency Comb OFDM Radar Systems

The frequency comb OFDM radar system described in [23], [24] shares some similarities with the proposed SA-OFDM radar system. Both systems introduce zero subcarriers between the active subcarriers, and both systems allow for a reduction of the ADC sampling frequency at the cost of a decreased maximum

unambiguous range $r_{\max}$. Besides that, there exist the following similarities and differences worth being discussed.

- Frequency comb OFDM radar system requires a comb of carrier frequencies for up- and down-conversion. On the one hand, this allows not only for a reduction of the ADC sampling frequency in the receiver, but also for a reduction of the DAC sampling frequency in the transmitter. On the other hand, generating a comb of carrier frequencies comes along with a significantly increased hardware complexity.
- As stated in [23], frequency comb OFDM is very sensitive to imperfectly calibrated amplitude and phase values of the spectral components of the frequency comb. An imperfect calibration leads to a reduced dynamic range and an increased peak-to-sidelobe ratio (PSLR). In contrast to that, SA-OFDM utilizes only a single carrier frequency, such that no amplitude or phase calibration is required.
- Concerning the impact of mutual interferences of different radar devices, SA-OFDM systems and frequency comb OFDM systems are expected to be affected in a similar way.

VI. Radar Measurement Results

This section presents the measurement results as well as an SNR comparison.

The system parameters correspond to that listed in Section IV-J. The measurements were conducted in a semi-anechoic chamber with two static corner reflectors (CRs) located at distances of 1.3 m and 4.1 m. The radar cross section of each of the CRs is 10 dBsm and both TX and RX are equipped with standard gain horn antennas each with a gain of 20 dBi. The baseband (BB) OFDM signal is generated by an arbitrary waveform generator (Keysight M8195 A) and up-converted to f_{c} by a Radiometer Physics ZRX90 module. The receiver consists of two low-noise amplifiers (LNAs) with a total gain of 40 dB and a noise figure of approx. 3 dB. The relatively high LNA gain is required to compensate the up- and down-conversion losses to and from f_{c}. Down-conversion of the RF-RX signal is realized in a spectrum analyzer (Rohde & Schwarz FSW85) and the BB-RX signal is digitized by a digital oscilloscope (Keysight DSO91204 A). All components are synchronized by a 10-MHz reference signal.

The obtained range profiles are shown in Fig. 6 for a standard OFDM radar system, an SA-OFDM radar system with $\kappa = 2$, and an SA-OFDM radar system with $\kappa = 4$.

Estimation of the SNR is carried out as described in Section IV-J. The SNR values obtained this way are 35.7 dB for the standard OFDM radar system, 32.6 dB for the SA-OFDM radar system with $\kappa = 2$, and 30.7 dB for the SA-OFDM radar system with $\kappa = 4$. The loss in SNR performance compared to the standard OFDM radar system is in accordance with the theoretical analysis carried out in Section IV-H.

VII. Subcarrier-Aliasing OFDM Communication System

This section focuses on the communication receiver of the proposed SA-OFDM joint radar and communication system. This communication receiver, naturally, can use the reduced ADC sampling frequency $f_{\mathrm{s}} = \frac{B}{\kappa}$, too. This entails a significant simplification of the design and implementation for the communication receiver ADC as well as for many follow-up processing steps.

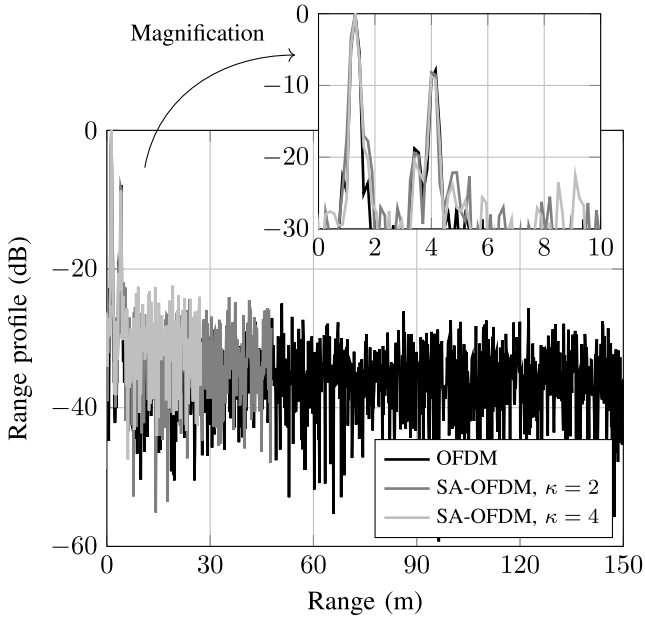

Fig. 6. Range profile for radar measurements with two corner reflectors. The curves are normalized to have 0 dB at the strongest reflection.

A side-effect of SA-OFDM is a reduced data rate compared to a standard OFDM communication system utilizing all N_{c} subcarriers. This may be considered a rather moderate disadvantage since the OFDM waveform allows for significantly higher data rates compared to, e.g., the frequency-modulated continuous wave (FMCW) waveform [29], [30].

This section begins with a discussion about the channel model, followed by the introduction of a so-called 'effective' channel. It will turn out that the effective channel representation allows employing well-known methods for channel estimation, synchronization and data estimation from standard OFDM communication systems.

A. Channel Model

Fig. 7 shows the basic transmitter signal processing chain as well as the first three receiver processing blocks for an SA-OFDM communication system. There, the transmit data in $\bar{\mathbf{S}}$ are mapped onto the active subcarriers with $\mu - 1$ zero subcarriers between them. After a transformation into time domain and an extension by the CP, the time domain signal is convolved with the complex BB channel impulse response (CIR). This CIR models the transmission from the transmit antenna to the receive antenna in BB. The receiver senses the signal with a reduced ADC sampling frequency, removes the CP, and performs a DFT to obtain the received active subcarriers. These active subcarriers are then sorted to restore the correct order. The shown processing blocks correspond to those already discussed for the radar receiver in Section III.

Fig. 7 indicates two different ways of representing the communication link as discussed in the following.

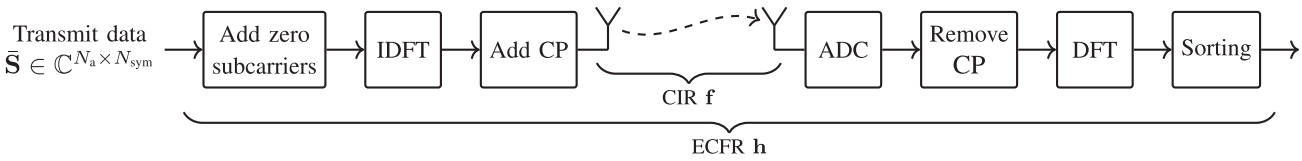

Fig. 7. Visualization of the CIR and the ECFR including the incorporated processing blocks. The analog front-end and the parallel-to-serial conversion are not shown.

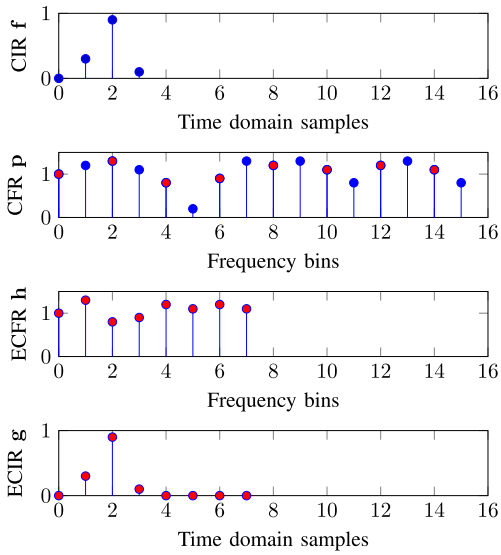

Fig. 8. Schematic visualization of the relation between the CIR, the CFR, ECFR, and the ECIR.

1) CIR Representation: The first way of modelling the transmission is to use the CIR between the transmit and the receive antenna. The CIR is denoted as $\mathbf{f} \in \mathbb{C}^{N_\mathbf{f}}$ of an assumed length $N_\mathbf{f} \leq N_c$.

Alternatively, a frequency domain representation of the CIR denoted as channel frequency response (CFR) $\mathbf{p} \in \mathbb{C}^{N_c}$ can be derived via

$$\mathbf{p} = \mathbf{F}_{N_c} \mathbf{B}_{zp} \mathbf{f}, \tag{27}$$

where $\mathbf{B}_{zp} \in \mathbb{C}^{N_c \times N_\mathbf{f}}$ is a matrix that zero-pads the CIR $\mathbf{f}$ to a length of N_c.

2) ECFR Representation: Note that the processing chain shown in Fig. 7 begins with the transmit subcarrier symbols for the active subcarriers and ends with the received subcarrier symbols at the active subcarriers in correct order. Hence, from a point of data estimation, it makes sense to combine all transformations and manipulations shown in Fig. 7 into one channel denoted as effective channel frequency response (ECFR). The derivation of the ECFR is described based on Fig. 8 for a simplified scenario. There, the first graph sketches an exemplary CIR $\mathbf{f}$ of length $N_\mathbf{f} = 4$. The corresponding CFR $\mathbf{p}$ has a length of $N_c = 16$, incorporates the channel coefficients for all subcarriers and is shown in the second graph of Fig. 8. The channel coefficients at the active subcarriers for an exemplary value of $\mu = 2$ are indicated in red color. The channel coefficients of the active subcarriers only (and in correct order) form an ECFR $\mathbf{h} \in \mathbb{C}^{N_a}$ depicted in the third graph. In this example, the ECFR has a length of $N_a = 8$. The time domain representation of the ECFR denoted as effective channel impulse response (ECIR) $\mathbf{g} \in \mathbb{C}^{N_a}$ is given as

$$\mathbf{g} = \mathbf{F}_{N_a}^{-1} \mathbf{h}. \tag{28}$$

Interestingly, if it holds that $N_c/\mu = N_a$, and if $N_\mathbf{f} \leq N_a$, the ECIR $\mathbf{g}$ is equivalent to the CIR $\mathbf{h}$ zero-padded to a length of N_a, which is proven in Appendix A. Hence, the ECIR $\mathbf{g}$ contains $N_a - N_\mathbf{f}$ zeros at the tail. This fact reduces the dimensionality of the channel estimation problem from N_a to $N_\mathbf{f}$, which can be beneficially exploited to increase the accuracy of the channel estimation [31]–[34].

B. Analogy to Standard OFDM Communication Systems

From a system point of view, an SA-OFDM communication system basically corresponds to a standard OFDM communication system when considering the ECFR as the frequency domain channel. This analogy comes along with some major simplifications discussed in the following.

The previously introduced ECFR models all processing blocks shown in Fig. 7. The blocks not shown in this figure are the encoder/decoder, the interleaver/deinterleaver, and the mapper/demapper. All these processing blocks may be re-used from standard OFDM communication systems [25], [35], [36] and are not introduced in detail in this work. Furthermore, a communication system in general requires methods for channel estimation, synchronization, and data estimation. These methods may be re-used from standard OFDM communication systems as well.

VIII. Simulation Setup and Performance Comparison

In this section, the simulation setup is introduced, and the BER performance of the proposed SA-OFDM communication system is compared to that of a standard OFDM communication system.

The system parameters of both systems are listed in Table I. The channel encoder utilizes a convolutional channel code with coding rate $r = 1/2$, constraint length 7 and the generator polynomials $(133, 171)_8$ in octal representation [33], [37]. The encoded bits are fed into a random interleaver whose block length is equal to the number of coded bits within an OFDM symbol. The interleaved bits are mapped onto QPSK symbols.

The channels are estimated using a standard method based on preamble OFDM symbols known to the receiver [32]–[34]. This method estimates the channel in time domain to reduce the dimensionality of the estimation problem (cf. Section VII-A).

TABLE I
SYSTEM PARAMETERS FOR THE STANDARD OFDM COMMUNICATION SYSTEM AND THE SA-OFDM COMMUNICATION SYSTEM

Parameter	Value
Bandwidth B	1 GHz
Carrier frequency f_c	77 GHz
Number of subcarriers N_c	1024
Number of OFDM symbols in a burst N_sym	512
Length of the cyclic prefix T_cp	1 µs
Number of DAC samples in the cyclic prefix N_cp	1000
Length of CIR $N_\mathbf{f}$	256
Number of preamble OFDM symbols	4
Number of pilot subcarriers	16

Synchronization aspects considered in this work are limited to Doppler shift induced effects and are implemented in the form of CPE estimation and compensation utilizing pilot subcarriers known to the receiver [33], [38]–[40]. Data estimation is performed using a linear minimum mean square error (LMMSE) estimator [31], [33], [41]. Since these methods are all well-known standard techniques, a detailed description is omitted in this work. The LMMSE output is transformed into soft information in form of log-likelihood ratios (LLRs) [42]–[44]. These LLRs are further fed into the deinterleaver and a Viterbi decoder [45].

The employed model for randomized CIR generation is described in [46]–[48]. A detailed description of this model is omitted in this work. The BER performances are evaluated by averaging over 5 000 line of sight (LOS) and 5 000 non-line of sight (NLOS) channels. These channels are quasi-static for the case of zero relative velocity, meaning that they stay constant during the transmission of one burst of N_sym OFDM symbols. For the considered case of non-zero relative velocity, which is drawn from a uniform distribution between ± 60 m/s, the channels are not quasi-static anymore, but superimposed by Doppler shift effects modelled in the form of ICI and CPE [33].

The considered standard OFDM communication system has a sampling frequency of $f_\mathrm{s} = B$, while the SA-OFDM communication system uses $f_\mathrm{s} = B/\kappa$ at the receiver. Assuming the same symbol alphabet and the same coding rate, this implies different data rates for the two systems. To achieve a fair comparison, the BER performances are compared for the same E_b/N_0 value measured before the ADC. E_b represents the average energy per bit of information, and $N_0/2$ indicates the double-sided noise power spectral density of a bandpass noise signal [33]. The time domain noise variance σ_n^2 follows as [49]

$$\sigma_\mathrm{n}^2 = \frac{P_\mathrm{s}}{(E_\mathrm{b}/N_0)\, r\, b\, \zeta\, \nu}, \tag{29}$$

where P_s represents the average power in time domain at the input of the ADC and b the number of coded bits per data symbol. Since only QPSK data symbols are considered, b is set to 2. The parameter ζ is defined as $\zeta = N_\mathrm{c}/(N_\mathrm{cp} + N_\mathrm{c})$ and accounts for the samples in the CP. ν accounts for the reduction in data rate due to potentially activating only a subset of subcarriers for data transmission. It is thus $\nu = 1$ for a standard OFDM system and $\nu = N_\mathrm{a}/N_\mathrm{c}$ for SA-OFDM. For a given E_b/N_0 value, the noise variance in SA-OFDM will thus be higher than in a standard OFDM system.

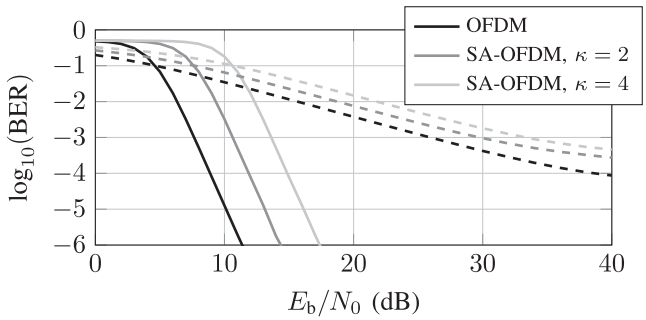

Fig. 9. BER performance for coded ($r = 1/2$, solid) and uncoded (dashed) transmission with perfect channel knowledge and perfect CPE synchronization.

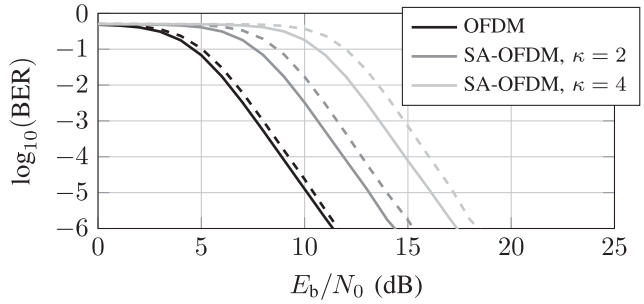

Fig. 10. BER performance for coded ($r = 1/2$) transmission with perfect CPE synchronization. The solid lines are with perfect channel knowledge, and the dashed lines are with imperfect channel estimation based on preamble OFDM symbols.

1) Perfect Channel Knowledge; Perfect CPE Synchronization: The first simulation scenario considers perfect channel knowledge and perfect CPE synchronization. Fig. 9 visualizes the resulting BER performances for coded and uncoded transmission. As expected, standard OFDM outperforms SA-OFDM. The loss in BER performance is approx. 3 dB for $\kappa = 2$, and by approx. 6 dB for $\kappa = 4$ measured for the coded case and at a BER of 10^{-4}.

In the remainder of this work, simulation results for the uncoded case are not shown anymore due to its limited practical relevance.

2) Perfect CPE Synchronization; Imperfect Channel Knowledge: For the second simulation, the channel is not perfectly known but estimated based on preamble OFDM symbols. The number of preamble OFDM symbols is set to 4 for both systems. The resulting BER performances are shown in Fig. 10, which also contains the BER performances for perfect channel knowledge from Fig. 9 as reference. As can be seen, the SA-OFDM communication system is slightly more affected by imperfect channel knowledge. However, the loss in BER performance can be considered to be low for both systems.

3) Perfect Channel Knowledge; Imperfect CPE Synchronization: For the third simulation, CPE synchronization is performed using pilot subcarriers, while the channel is perfectly known to the receiver. The resulting BER performances when employing 16 pilot subcarriers are shown in Fig. 11 together

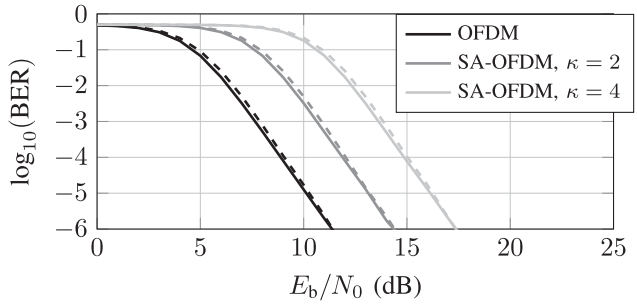

Fig. 11. BER performance for coded ($r = 1/2$) transmission with perfect channel knowledge. The solid lines are with perfect CPE synchronization, and the dashed lines are with imperfect CPE synchronization based on pilot subcarriers.

with the BER performances for the case of perfect CPE synchronization from Fig. 9. It turns out that the loss in BER due to imperfect CPE synchronization is minimal for both systems.

IX. Conclusion

In this work, a novel joint radar and communication system denoted as SA-OFDM was proposed. The main advantage of SA-OFDM over a standard OFDM joint radar and communication system is that it allows for reducing the ADC sampling frequency in the receiver without sacrificing range resolution. This advantage leads to a simplified design and implementation of the ADC and follow-up processing blocks. Disadvantages of SA-OFDM over a standard OFDM joint radar and communication system include a reduced maximum unambiguous range and a lower SNR in the RDM. Compared to stepped-carrier OFDM, a clear drawback of SA-OFDM is that it does not allow for a reduction of the DAC sampling frequency in the transmitter as it does for the ADC in the receiver. However, a clear advantage of SA-OFDM over stepped-carrier OFDM is that it simplifies simultaneous communication and radar sensing.

The theoretical analysis of SA-OFDM for the radar sensing task was supplemented and completed by radar measurements. For the communication task, it was shown that essential processing blocks of the transmitter and the receiver can be represented by a so-called effective channel. This effective channel representation allowed employing well-known methods for channel estimation, synchronization and data estimation from standard OFDM communications systems also for SA-OFDM systems. The performances of these methods were analyzed by means of BER simulations.

Appendix A
Derivation of the Relationship Between CIR and ECIR

This appendix analyzes the relation between the CIR $\mathbf{f} \in \mathbb{C}^{N_\mathbf{f}}$ and the ECIR $\mathbf{g} \in \mathbb{C}^{N_\mathrm{a}}$ introduced in Section VII-A.

Recall that $\mathbf{f} \in \mathbb{C}^{N_\mathbf{f}}$ is a time domain vector representing the CIR between the transmit antenna and the receive antenna. The CFR $\mathbf{p} \in \mathbb{C}^{N_\mathrm{c}}$ is a frequency domain vector containing the frequency response for all N_c subcarriers. $\mathbf{h} \in \mathbb{C}^{N_\mathrm{a}}$ is the ECFR and contains the frequency response of the N_a active subcarriers. The ECIR $\mathbf{g} \in \mathbb{C}^{N_\mathrm{a}}$ is the time domain version of the ECFR.

The ECIR $\mathbf{g} \in \mathbb{C}^{N_\mathrm{a}}$ can be derived in vector representation from the ECFR $\mathbf{h} \in \mathbb{C}^{N_\mathrm{a}}$ according to (28). Hence, the nth element of $\mathbf{g}$ is given by

$$[\mathbf{g}]_n = \frac{1}{N_\mathrm{a}} \sum_{k=0}^{N_\mathrm{a}-1} [\mathbf{h}]_k \, \exp\left(\mathrm{j}2\pi \frac{kn}{N_\mathrm{a}}\right) \quad \text{for } 0 \le n < N_\mathrm{a}. \tag{30}$$

The kth element of $\mathbf{h}$, denoted as $[\mathbf{h}]_k$, on the other hand can be obtained from the CFR $\mathbf{p} \in \mathbb{C}^{N_\mathrm{c}}$ according to

$$[\mathbf{h}]_k = [\mathbf{p}]_{\mu k} \quad \text{for } 0 \le k < N_\mathrm{a}. \tag{31}$$

By reformulating (27), the scalars $[\mathbf{p}]_{\mu k}$ can be identified to be

$$[\mathbf{p}]_{\mu k} = \sum_{m=0}^{N_\mathbf{f}-1} [\mathbf{f}]_m \, \exp\left(-\mathrm{j}2\pi \frac{\mu k m}{N_\mathrm{c}}\right) \quad \text{for } 0 \le k < N_\mathrm{a}. \tag{32}$$

Combining (30)–(32) allows for

$$[\mathbf{g}]_n = \frac{1}{N_\mathrm{a}} \sum_{k=0}^{N_\mathrm{a}-1} \left(\sum_{m=0}^{N_\mathbf{f}-1} [\mathbf{f}]_m \, \exp\left(-\mathrm{j}2\pi \frac{\mu k m}{N_\mathrm{c}}\right)\right) \cdot \exp\left(\mathrm{j}2\pi \frac{kn}{N_\mathrm{a}}\right) \tag{33}$$

$$= \frac{1}{N_\mathrm{a}} \sum_{k=0}^{N_\mathrm{a}-1} \sum_{m=0}^{N_\mathbf{f}-1} [\mathbf{f}]_m \, \exp\left(\mathrm{j}2\pi k \left(\frac{n}{N_\mathrm{a}} - \frac{\mu m}{N_\mathrm{c}}\right)\right) \tag{34}$$

$$= \frac{1}{N_\mathrm{a}} \sum_{m=0}^{N_\mathbf{f}-1} [\mathbf{f}]_m \underbrace{\left(\sum_{k=0}^{N_\mathrm{a}-1} \exp\left(\mathrm{j}2\pi k \left(\frac{n}{N_\mathrm{a}} - \frac{\mu m}{N_\mathrm{c}}\right)\right)\right)}_{s(n,m)} \tag{35}$$

$$= \frac{1}{N_\mathrm{a}} \sum_{m=0}^{N_\mathbf{f}-1} [\mathbf{f}]_m \, s(n,m). \tag{36}$$

The scalar $s(n,m) \in \mathbb{C}$ depends on μ, N_c, and N_a, and is analyzed for two cases.

The first case is when $N_\mathrm{c}/\mu = N_\mathrm{a}$, for which $s(n,m)$ is a scaled Dirac delta function $s(n,m) = N_\mathrm{a}\, \delta[(n-m)\%N_\mathrm{a}]$. Thus, it follows that the observed ECIR corresponds to

$$[\mathbf{g}]_n = \sum_{m=0}^{N_\mathbf{f}-1} [\mathbf{f}]_m \, \delta\left[(n-m)\,\%N_\mathrm{a}\right] \tag{37}$$

with $0 \le n < N_\mathrm{a}$. A further simplification is observed when $N_\mathbf{f} \le N_\mathrm{a}$, for which it holds that

$$[\mathbf{g}]_n = [\mathbf{f}]_n \quad \text{for } 0 \le n < N_\mathbf{f}, \tag{38}$$

and $[\mathbf{g}]_n = 0$ for $N_\mathbf{f} \le n < N_\mathrm{a}$. Thus, in this scenario, the ECIR is equivalent to the CIR zero-padded to a length of N_a.

The second case is when $N_\mathrm{c}/\mu \neq N_\mathrm{a}$, for which $s(n,m)$ is not a scaled Dirac delta function anymore. Then, the ECFR $\mathbf{g}$ corresponds to the CIR $\mathbf{f}$ distorted by windowing effects, and can be derived via (35).

REFERENCES

[1] N. Levanon, "Multifrequency complementary phase-coded radar signal," *IEE Proc. - Radar, Sonar Navigat.*, vol. 147, no. 6, pp. 276–284, 2000.

[2] B. J. Donnet and I. D. Longstaff, "Combining MIMO radar with OFDM communications," in *Proc. IEEE Eur. Radar Conf.*, 2006, pp. 37–40.

[3] C. Sturm, E. Pancera, T. Zwick, and W. Wiesbeck, "A novel approach to OFDM radar processing," in *Proc. IEEE Radar Conf.*, 2009, pp. 1–4.

[4] G. Hakobyan and B. Yang, "A novel inter carrier-interference free signal processing scheme for OFDM radar," *IEEE Trans. Veh. Technol.*, vol. 67, no. 6, pp. 5158–5167, Jun. 2018.

[5] Y. L. Sit and T. Zwick, "Automotive MIMO OFDM radar: Subcarrier allocation techniques for multiple-user access and DOA estimation," in *Proc. IEEE 11th Eur. Radar Conf.*, 2014, pp. 153–156.

[6] D. Garmatyuk, J. Schuerger, Y. T. Morton, K. Binns, M. Durbin, and J. Kimani, "Feasibility study of a multi-carrier dual-use imaging radar and communication system," in *Proc. IEEE Eur. Microw. Conf.*, 2007, pp. 1473–1476.

[7] G. Hakobyan and B. Yang, "A novel OFDM-MIMO radar with non-equidistant subcarrier interleaving and compressed sensing," in *Proc. IEEE 17th Int. Radar Symp.*, 2016, pp. 1–5.

[8] C. Sturm, T. Zwick, and W. Wiesbeck, "An OFDM system concept for joint radar and communications operations," in *Proc. IEEE 69th Veh. Technol. Conf.*, 2009, pp. 1–5.

[9] C. Sturm, T. Zwick, W. Wiesbeck, and M. Braun, "Performance verification of symbol-based OFDM radar processing," in *Proc. IEEE Radar Conf.*, 2010, pp. 60–63.

[10] M. Braun, C. Sturm, A. Niethammer, and F. K. Jondral, "Parametrization of joint OFDM-based radar and communication systems for vehicular applications," in *Proc. IEEE 20th Int. Symp. Pers., Indoor, Mobile Radio Commun.*, 2009, pp. 3020–3024.

[11] O. Lang, A. Onic, C. Schmid, R. Feger, and M. Huemer, "Reducing hardware requirements and computational effort for automotive OFDM radar systems," in *Proc. IEEE 54th Asilomar Conf. Signals, Syst., Comput.*, 2020, pp. 1563–1567.

[12] G. Lellouch, R. Pribic, and P. van Genderen, "Frequency agile stepped OFDM waveform for HRR," in *Proc. IEEE Int. Waveform Diversity Des. Conf.*, 2009, pp. 90–93.

[13] B. Schweizer, D. Schindler, C. Knill, J. Hasch, and C. Waldschmidt, "On hardware implementations of stepped-carrier OFDM radars," in *Proc. IEEE/MTT-S Int. Microw. Symp.*, 2018, pp. 891–894.

[14] B. Schweizer, D. Schindler, C. Knill, and C. Waldschmidt, "A doppler-tolerant stepped-carrier OFDM-Radar scheme based on all-cell-doppler-correction," in *Proc. IEEE 20th Int. Radar Symp.*, 2019, pp. 1–9.

[15] C. Pfeffer, R. Feger, and A. Stelzer, "A stepped-carrier 77-GHz OFDM MIMO radar system with 4 GHz bandwidth," in *Proc. IEEE Eur. Radar Conf. IEEE*, 2015, pp. 97–100.

[16] G. Lellouch, A. K. Mishra, and M. Inggs, "Stepped OFDM radar technique to resolve range and doppler simultaneously," *IEEE Trans. Aerosp. Electron. Syst.*, vol. 51, no. 2, pp. 937–950, Apr. 2015.

[17] B. Schweizer, D. Schindler, C. Knill, J. Hasch, and C. Waldschmidt, "Expanding the unambiguous velocity limitation of the stepped-carrier OFDM radar scheme," in *Proc. IEEE 15th Eur. Radar Conf.*, 2018, pp. 22–25.

[18] K. Huo, B. Deng, Y. Liu, W. Jiang, and J. Mao, "The principle of synthesizing HRRP based on a new OFDM phase-coded stepped-frequency radar signal," in *Proc. IEEE 10th Int. Conf. Signal Process.*, 2010, pp. 1994–1998.

[19] B. Schweizer, C. Knill, D. Schindler, and C. Waldschmidt, "Stepped-carrier OFDM-Radar processing scheme to retrieve high-resolution range-velocity profile at low sampling rate," *IEEE Trans. Microw. Theory Tech.*, vol. 66, no. 3, pp. 1610–1618, Mar. 2018.

[20] A. Zandieh, S. Bonen, M. S. Dadash, M. J. Gong, J. Hasch, and S. P. Voinigescu, "155 GHz FMCW and stepped-frequency carrier OFDM radar sensor transceiver IC featuring a PLL with $<$30 ns settling time and 40 fs rms jitter," *IEEE Trans. Microw. Theory Tech.*, vol. 69, no. 11, pp. 4908–4924, Nov. 2021.

[21] D. Schindler, B. Schweizer, C. Knill, J. Hasch, and C. Waldschmidt, "An integrated stepped-carrier OFDM MIMO radar utilizing a novel fast frequency step generator for automotive applications," *IEEE Trans. Microw. Theory Tech.*, vol. 67, no. 11, pp. 4559–4569, Nov. 2019.

[22] D. Schindler, B. Schweizer, C. Knill, J. Hasch, and C. Waldschmidt, "MIMO-OFDM radar using a linear frequency modulated carrier to reduce sampling requirements," *IEEE Trans. Microw. Theory Techn.*, vol. 66, no. 7, pp. 3511–3520, Jul. 2018.

[23] B. Nuss, J. Mayer, S. Marahrens, and T. Zwick, "Frequency comb OFDM radar system with high range resolution and low sampling rate," *IEEE Trans. Microw. Theory Techn.*, vol. 68, no. 9, pp. 3861–3871, Sep. 2020.

[24] B. Nuss, L. G. de Oliveira, and T. Zwick, "Frequency comb MIMO OFDM radar with nonequidistant subcarrier interleaving," *IEEE Microw. Wireless Compon. Lett.*, vol. 30, no. 12, pp. 1209–1212, Dec. 2020.

[25] R. van Nee and R. Prasad, *OFDM for Wireless Multimedia Communications, Ser. Artech House Universal Personal Communications Library*. Norwood, MA, USA: Artech House, 2000.

[26] T. Jiang and Y. Wu, "An overview: Peak-to-average power ratio reduction techniques for OFDM signals," *IEEE Trans. Broadcast.*, vol. 54, no. 2, pp. 257–268, Jun. 2008.

[27] G. M. Brooker, "Mutual interference of millimeter-wave radar systems," *IEEE Trans. Electromagn. Compat.*, vol. 49, no. 1, pp. 170–181, Feb. 2007.

[28] M. Toth, P. Meissner, A. Melzer, and K. Witrisal, "Performance comparison of mutual automotive radar interference mitigation algorithms," in *Proc. IEEE Radar Conf.*, 2019, pp. 1–6.

[29] F. Uysal, "Phase-coded FMCW automotive radar: System design and interference mitigation," *IEEE Trans. Veh. Technol.*, vol. 69, no. 1, pp. 270–281, Jan. 2020.

[30] M. B. Alabd, L. G. de Oliveira, B. Nuss, W. Wiesbeck, and T. Zwick, "Time-frequency shift modulation for chirp sequence based radar communications," in *Proc. IEEE MTT-S Int. Conf. Microw. Intell. Mobility*, 2020, pp. 1–4.

[31] S. M. Kay, *Fundamentals of Statistical Signal Processing: Estimation Theory*. Englewood Cliffs, NJ, USA: Prentice Hall, 1993, vol. 1.

[32] O. Lang, "Knowledge-aided methods in estimation theory and adaptive filtering," Ph.D. dissertation, Inst. Sig. Process., Johannes Kepler University Linz, Austria, 2018.

[33] C. Hofbauer, "Design and analysis of unique word OFDM," Ph.D. dissertation, Inst. Netw. Embedded Syst., Alpen-Adria-University Klagenfurt, Austria, 2016. [Online]. Available: https://permalink.obvsg.at/UKL/AC12608830

[34] M. Huemer and O. Lang, "On component-wise conditionally unbiased linear bayesian estimation," in *Proc. IEEE 48th Asilomar Conf. Signals,Syst., Comput.*, 2014, pp. 879–885.

[35] S. Haykin, *Digital Communication Systems*. Hoboken, NJ, USA: Wiley, 2013.

[36] M. Salehi and J. Proakis, *Digital Communications*. New York, NY, USA: McGraw-Hill Education, vol. 31, p. 32, 2007.

[37] *Part 11: Wireless LAN Medium Access Control (MAC) and Physical Layer (PHY) Specifications. High-speed Physical Layer in the 5 GHz Band*, IEEE Computer Society LAN/MAN Standards Committee, IEEE Std 802.11a-1999(R2003), Dec. 1999.

[38] F. Classen and H. Meyr, "Frequency synchronization algorithms for OFDM systems suitable for communication over frequency selective fading channels," in *Proc. IEEE Veh. Technol. Conf.*, 1994, pp. 1655–1659.

[39] C. Hofbauer, W. Haselmayr, H.-P. Bernhard, and M. Huemer, "Impact of a carrier frequency offset on unique word OFDM," in *Proc. IEEE 31st Annu. Int. Symp. Pers., Indoor Mobile Radio Commun.*, London, U.K., 2020, pp. 1–7.

[40] C. Hofbauer, W. Haselmayr, H.-P. Bernhard, and M. Huemer, "On the inclusion and utilization of pilot tones in unique word OFDM," *IEEE Trans. Signal Process.*, vol. 68, pp. 5504–5518, 2020.

[41] M. Huemer, A. Onic, and C. Hofbauer, "Classical and bayesian linear data estimators for unique word OFDM," *IEEE Trans. Signal Process.*, vol. 59, no. 12, pp. 6073–6085, Dec. 2011.

[42] S. Allpress, C. Luschi, and S. Felix, "Exact and approximated expressions of the log-likelihood ratio for 16-QAM signals," in *Proc. IEEE 38th Asilomar Conf. Signals, Syst., Comput.*, 2004, pp. 794–798.

[43] W. Haselmayr, O. Lang, A. Springer, and M. Huemer, "Does vector gaussian approximation after LMMSE filtering improve the LLR quality?," *IEEE Signal Process. Lett.*, vol. 24, no. 11, pp. 1676–1680, Nov. 2017.

[44] O. Lang, M. Huemer, and C. Hofbauer, "On the log-likelihood ratio evaluation of CWCU linear and widely linear MMSE data estimators," in *Proc. IEEE 50th Asilomar Conf. Signals, Syst., Comput.*, 2016, pp. 633–637.

[45] A. Viterbi, "Error bounds for convolutional codes and an asymptotically optimum decoding algorithm," *IEEE Trans. Inf. Theory*, vol. 13, no. 2, pp. 260–269, Apr. 1967.

[46] M. K. Samimi and T. S. Rappaport, "Statistical channel model with multi-frequency and arbitrary antenna beamwidth for millimeter-wave outdoor communications," in *Proc. IEEE Globecom Workshops*, 2015, pp. 1–7.

[47] M. K. Samimi and T. S. Rappaport, "3-D millimeter-wave statistical channel model for 5G wireless system design," *IEEE Trans. Microw. Theory Tech.*, vol. 64, no. 7, pp. 2207–2225, Jul. 2016.
[48] N. WIRELESS, "Open source downloadable 5G channel simulator software," Accessed: Aug. 2020. [Online]. Available: http://bit.ly/1WNPpDX
[49] W. Zhang and M. J. Miller, "Baseband equivalents in digital communication system simulation," *IEEE Trans. Educ.*, vol. 35, no. 4, pp. 376–382, Nov. 1992.

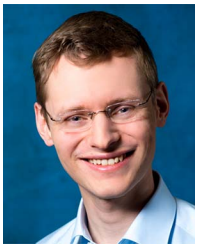

Oliver Lang (Member, IEEE) received the bachelor's degree in electrical engineering and information technology and the master's degree in microelectronics from the Vienna University of Technology, Vienna, Austria, in 2011 and 2014, respectively, and the Ph.D. degree from the Institute of Signal Processing, Johannes Kepler University (JKU), Linz, Austria, in 2018. From 2014 to 2018, he was a Member of the Institute of Signal Processing, Johannes Kepler University. From 2018 to 2019, he was with DICE GmbH in Linz, which was a subsidiary Company of Infineon Austria GmbH. During this period, he worked on automotive radar MMICs and systems. Since March 2019, he has been a University Assistant with Ph.D. with the Institute of Signal Processing, JKU. He is also a main inventor of several patents and patent applications in the field of automotive radar systems and main author of several publications in the field of estimation theory and adaptive filtering.

Reinhard Feger was born in Kufstein, Austria, in 1980. He received the Dipl.-Ing. (M.Sc.) degree in mechatronics and the Dr. Techn. (Ph.D.) degree in mechatronics from Johannes Kepler University Linz, Linz, Austria, in 2005 and 2010, respectively. In 2005, he joined the Institute for Communications and Information Engineering, Johannes Kepler University Linz, as a Research Assistant. In 2007, he became a Member of the Christian Doppler Laboratory for Integrated Radar Sensors, Johannes Kepler University Linz. He is currently an Associate Professor with the Institute for Communications Engineering and RF-Systems, Johannes Kepler University Linz. His research interests include radar signal processing, and radar system design for industrial and automotive radar sensors. Dr. Feger was the recipient of the 2011 Microwave Prize and 2011 German Microwave Conference Best Paper Award, and Best Measurement Paper Prize at the European Conference on Antennas and Propagation in 2012.

Christian Hofbauer (Member, IEEE) received the master's degree in hardware/software systems engineering from the University of Applied Sciences Upper Austria, Hagenberg, Austria, and the Ph.D. degree in information technology from Klagenfurt University, Klagenfurt, Austria. He is currently a Senior Scientist with Wireless Communications Group, Silicon Austria Labs. His main research interests include wireless communication systems, adaptive and statistical signal processing, and system architectures for mobile devices. He is also a Member of the IEEE Signal Processing Society and German Society of Information. Together with his colleagues, he was the recipient of the German EEEfCOM Innovation Award for the development of the Unique Word OFDM signaling scheme in 2010.

Mario Huemer (Senior Member, IEEE) received the Dipl.-Ing. and Dr.tech. degrees from Johannes Kepler University (JKU) Linz, Linz, Austria, in 1996 and 1999, respectively. After holding positions in industry and academia, he became an Associate Professor with the University of Erlangen–Nuremberg, Erlangen, Germany, from 2004 to 2007, and a Full Professor with Klagenfurt University, Klagenfurt, Austria, from 2007 to 2013. Since September 2013, he has been heading the Institute of Signal Processing, JKU Linz, as a Full Professor, and since 2017, he has been the Co-Head of the Christian Doppler Laboratory for Digitally Assisted RF Transceivers for Future Mobile Communications. His research interests include statistical and adaptive signal processing, signal processing architectures, and mixed signal processing with applications in information and communications engineering, radio frequency transceivers for communications and radar, sensor, and biomedical signal processing. He was the recipient of the dissertation awards of the German Society of Information Technology (ITG) and Austrian Society of Information and Communications Technology, respectively, Austrian Kardinal Innitzer Award in Natural Sciences, and German ITG Award.